

AERODYNAMIC INVESTIGATION BY EXPERIMENTAL AND COMPUTATIONAL SIMULATION OF A FLYING WING UNMANNED AERIAL VEHICLE FOR CARGO DELIVERY AND SURVEILLANCE MISSIONS

Atikah Basyirah ABDUL MUTA'ALI , Rizal Effendy MOHD NASIR  , Wahyu KUNTJORO 

Flight Technology and Test RIG, School of Mechanical Engineering, College of Engineering, Universiti Teknologi MARA (UiTM), 40450 Shah Alam, Selangor, Malaysia

Article History:

- received 23 April 2024
- accepted 10 September 2024

Abstract. Baseline-IX is a tailless aircraft design with compound wing attached to a short body, a transition between a straight, swept flying wing design and a blended wing-body. Baseline-IX planform was designed to deal with a small BWB UAV that is capable of cargo delivery and surveillance missions. The design is influenced by the requirement of cargo space to carry batteries medical and other emergency supplies in its fuselage with a nose-mounted mission camera with a wingspan under 2.0 meters. This paper focuses on studying the aerodynamic characteristics of the novel Baseline-IX, inspired by its predecessor, the Baseline-V. Aerodynamic characteristics of Baseline-IX were investigated and validated through numerical computational simulations and wind tunnel experiments. The maximum lift-to-drag ratio of Baseline-IX obtained through this study is 15.14 for 1:2.4 scaled model and 17.46 for 1:1 prototype. Numerical simulation and wind tunnel experiments' lift-to-drag ratio percentage difference is 4.92%. Baseline-IX's lift-to-drag ratio surpasses 14.09% and 24.28% over similar-missions UAV operating in the market while both are larger in size. Baseline-IX has the potential to be developed as a small, easy to carry cargo delivery and surveillance BWB UAV.

Keywords: tail-less compound wing-body, blended wing-body, unmanned aerial vehicle, wind tunnel experiment, aerodynamics.

 Corresponding author. E-mail: rizal524@uitm.edu.my

1. Introduction

Blended wing-body (BWB) is a fixed-wing aircraft with its wings and fuselage merged smoothly resulting in some designs almost resemble a pure flying wing. Compared to classic tube-and-wing (TAW) design, the unconventional configuration's main advantages are high aerodynamic efficiency and the ability to deploy a significant amount of lift for the same flying conditions (Jemitola & Okonwo, 2022). It has been quantified that 2–3% of total atmospheric emissions are contributed through commercial aviation and has kickstarted the research on alternative, fuel-friendly aircraft configuration (Aprovitola et al., 2022; Dimitriou et al., 2022). The issue of reducing the weight of aircraft components has recently been widely addressed in helping to reduce power consumption. In addition to structural changes, researchers are developing and using new materials, especially composite materials. These materials are required to have at least similar mechanical properties to those previously used and to reduce weight significantly (Karpenko et al., 2023; Karpenko & Nugaras, 2022) has presented analyses of the dynamic properties of the new materials used for the wings of flying objects.

BWB showed remarkable performance improvements compared to conventional aircraft, including a 15% reduction in take-off weight and a 27% reduction in fuel burn per seat mile (Liebeck, 2004). The conventional tube-and-wing configuration has 33% more total surface area (BWB) configuration that has lower wetted area and lower drag (Ammar et al., 2017; Li et al., 2012; Liebeck, 2004; Okonkwo & Smith, 2016). This opens potential for efficient cargo or surveillance under UAV development.

Chen et al. (2019) mentioned that BWB concepts can be put into three categories. First, BWB with double swept planform and a short aft-body, secondly a Hybrid Wing Body (HWB) that has leading-edge carving over the centre body, and Integrated Wing Body (IWB) which is more conventional with an extended aft-body (Chen et al., 2019). BWB concepts over the years of research have encouraged trade-offs between different disciplines to make it work (Dehpanah & Nejat, 2015; Dimitriou et al., 2022; Liebeck, 2004; Mohammad Zadeh & Sayadi, 2018).

Aside from a fully blended BWB planform, a practical approach by Jemitola and Okonkwo, stated that a box-wing configuration offers lower design risk than a BWB due to its less radical change from conventional aircraft

configuration (Jemitola & Okonwo, 2022). This phase gradually implements blended wing-body to airframe designs before evolving into smoothly BWB planform. Papadopoulos et al. (2022) said that the combination of BWB and box-wing planform has its own advantages. BWB planform offers aerodynamics advantage while box-wing planform offers more cargo space (Papadopoulos et al., 2022).

Fraction-in-size BWB UAVs can move swiftly and serve different purposes not only limited to cargo transfer but for mapping, filming, small cargo delivery, and surveillance and reconnaissance (Dimitriou et al., 2022). This BWB UAV design has a wingspan of between 1.0 meters to 3.0 meters. Zeng et al. (2020) studied 4 different aerodynamic optimization scenarios of their BITU BWB while Wau Bulan UAV by Kusumohadi et al. (2021) in early conceptual phase has incorporated wau bulan shape into their Wau Bulan UAV planform (Kusumohadi et al., 2021; Zeng et al., 2020). Raja et al. (2023) optimizes computational aerodynamics and control investigations on their VTOL Hybrid BWB UAV. Arora et al investigate aerodynamics over BWB with different airfoil at different station through computational analysis and wind tunnel experiment (Arora et al., 2023).

There are few blended-wing body UAV studies that consider cargo space payload delivery. DEALER UAS with mission profile of emergency supplies delivery has a wingspan of 7.15 meters (Kapsalis et al., 2021). 3.0 meters wingspan Zipline UAV (Zipline, 2022) also has similar mission profile of cargo and surveillance to Baseline-IX.

There is a gap study of small BWB UAV design with the purpose of quick emergency reaction and short distance missions. This paper focuses on the preliminary design phase of the application of a 2.0 meters wingspan of a small cargo delivery and surveillance BWB UAV for emergency missions. Progression from fully BWB planform to a compound wing-body for ease in logistics. Aerodynamics performance obtained through numerical computational analysis is always practiced, but in this paper, a wind tunnel experiment is added for validation purpose. The findings and methodology shared within this paper will benefit aerodynamicists working on a similar planform and provide knowledge on the preliminary design process of a BWB.

2. Baseline-IX design configuration

Baseline-IX’s cargo delivery missions are targeted for medical kit and food supplies deliveries during emergencies such as first aid kit, heat blanket, batteries, and energy food bars. These supplies will help victims stranded within areas that can be quickly accessible by Baseline-IX before being rescued by local authorities. Baseline-IX will also be able to provide surveillance assistance to local authorities with every cargo delivery mission. Baseline-IX as a UAV with cargo delivery and surveillance mission profile shown in Figure 1.

Based on research, currently there is a gap for UAV of cargo delivery and surveillance mission that is within the size of under 2.0 meters. DELAER RX-3 and Zipline Platform 1 were chosen as unmanned aerial vehicles that are similar in mission profile and have comparable wingspans. Zipline platform 1 is a fixed-wing, long-range cargo delivery UAV that started out as the first medical logistics service originated in Rwanda (Zipline, 2022). Baseline-IX UAV’s wingspan is a bit over half of Zipline’s wingspan which requires more width of runway/take off space. Baseline-IX is estimated to carry 20% more payload mass compared to Zipline.

DELAER RX-3 is a BWB UAV with a wingspan just over 7.0 meters which is 4 times the size of Baseline-IX UAV. DELAER RX-3 is designed for maximum weight of 40 kg cargo delivery and surveillance missions (Kapsalis et al., 2021). Baseline-IX and DELAER RX-3 share similar cargo delivery and surveillance missions. However, due to size, DELAER RX-3 is not easy to transport and requires a bigger hangar. Specification of said UAVs is summarized in Table 1.

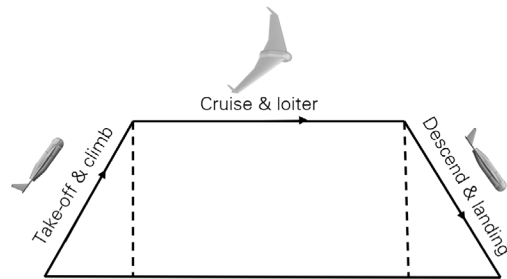


Figure 1. Baseline-IX BWB anticipated mission profile

Table 1. UAV with similar mission to Baseline-IX

Cargo UAV	 Baseline-IX UAV	 DELAER RX-3 (Kapsalis et al., 2021)	 Zipline Platform 1 (Zipline, 2022)
Mission	Cargo delivery and surveillance	Cargo delivery and surveillance	Cargo delivery and surveillance
Wingspan (m)	1.74	7.15	3.00
Payload mass (kg)	2.0	40.0	1.8
Cruising speed (km/h)	54	180	101
Delivery mechanism	Parachute-floating delivery	Airdrop/airland	Parachute-controlled floating delivery

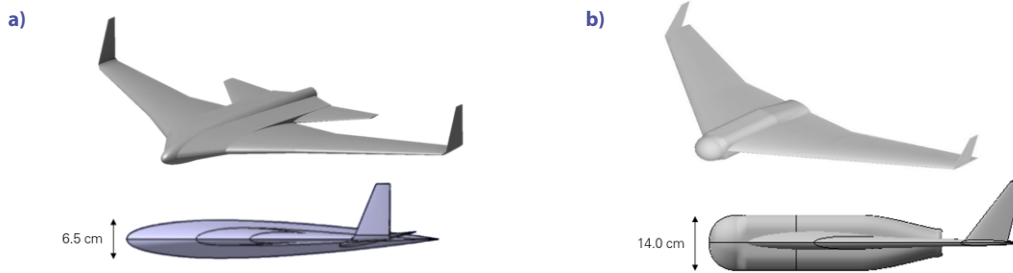


Figure 2. Flight Technology and Test Centre's BWB designs: a – Baseline-V BWB; b – Baseline-IX BWB

Baseline-IX is an upgrade from Baseline-V (blended wing-body and tail). The previous design lack large usable volume to include cargo in their missions. Scaling up seems to be the option for more cargo space but it will demand a bigger storage room or hangar. Baseline-IX was designed differently from its predecessors to fulfill its mission profile purpose. Both Baseline-IX and Baseline-V are shown in Figure 2.

Baseline-IX took a practical approach to serve its purpose by extending a simpler planform with wing design pulled from Baseline-V (compound wing) and adapting tail-less configuration. Compared to its predecessor, it has a shorter but larger fuselage in the middle, with moderate blending to the wings, and slightly higher wing aspect ratios. Baseline-IX has taken a little less radical approach than its predecessor, Baseline-V which took a fully BWB configuration. Jemitola and Okonkwo (Jemitola & Okonkwo, 2022) stated that a practical approach of a box-wing configuration offers lower design risk than a BWB due to its less radical change from conventional aircraft configuration. Baseline-IX's nose design is heavily influenced by a stabilized gimbal camera to be carried, seen in Figure 3. The compound wing is generated from an MH60 airfoil which is attached to its nearly box-shaped fuselage.

As mentioned previously, Baseline-IX prototype shown in Figure 3 below was built on the idea of surveillance and cargo delivery missions. Through modular design method the usage of cargo volume was adapted. The finalized design is simple and practical for easy, quick manufacturing and repair downtime. The fuselage cargo space was designed to place important UAS systems and to arrange the emergency supplies as shown in Figure 4. The proposed idea is the emergency supplies are stored in a crash-proof, wet-proof case and dropped at precise locations by para-



Figure 3. Baseline-IX BWB UAV Prototype

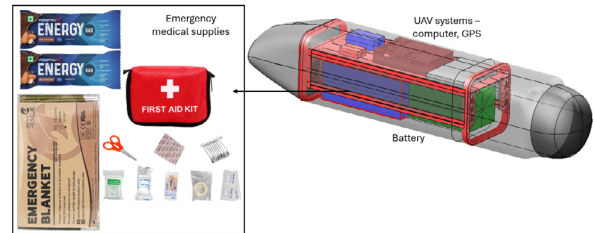


Figure 4. Proposed cargo space usage for Baseline-IX BWB

Table 2. Specifications of Baseline-IX BWB

Specifications	Baseline-IX BWB Prototype
Mean Aerodynamic Chord (m)	0.356
Wingspan (m)	1.74
Wing Area (m ²)	0.468

chute-controlled mechanism. The drop door on the belly of Baseline-IX will be controlled as well.

MH60 airfoil was chosen due to its low moment coefficient suitable for tailless aircraft and with a relatively high maximum lift coefficient. It is designed under 2.0 meters wingspan for ease in logistics. The wingspan allows Baseline-IX to easily be carried by hand and fit in most vans and trucks for urgent and quick cargo missions. Table 2 shows the specifications of Baseline-IX BWB prototype.

3. Methodology

New BWB planforms will go through the preliminary aerodynamic analysis and drag reduction study (Chen et al., 2019; Li et al., 2012; Mohammad Zadeh & Sayadi, 2018). Afterwards, the practice goes through an evaluation which includes control, stability, and trimming of the BWB by using conventional or new technology (Chen et al., 2019; Mohammad Zadeh & Sayadi, 2018; Panagiotou et al., 2022; Qin et al., 2004). Performance evaluated are lift-to-drag ratio, followed by fuel consumption, range and take-off distance, including the static margin (Viviani et al., 2020). Studies on flying characteristics of an aircraft involve wind tunnel experiments, computational simulations, and prototype flight tests to develop an aerodynamic model (Wang et al., 2020; Waters et al., 2013). These experiments and simulations reduce risks of

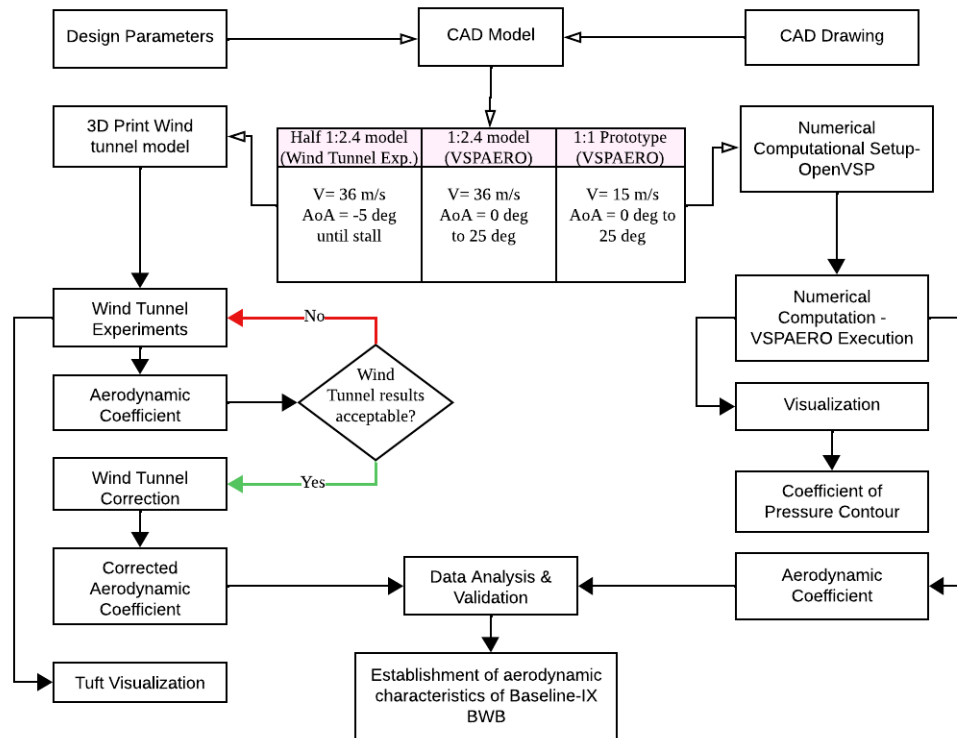


Figure 5. Flowchart of methodology on the study of Baseline-IX BWB

a flight test and shorten the development cycle by reducing the number of prototype trials (Wang et al., 2020).

The research methodology flowchart is shown in Figure 5. First, was to determine the mission for the BWB platform. With the intention to carry cargo/payload and ease of transport, the design revolves around the mission profile. To understand the aerodynamic performance of Baseline-IX BWB, the platform was investigated by using three different experiments. Firstly, a half 3-D printed scaled-down wind tunnel model to be tested in wind tunnel facility. Secondly, a similar scaled-down model to be simulated by VSPAERO. Lastly, prototype-sized model which is simulated by VSPAERO as well.

Both simulated and experimental studies were conducted on the Baseline-IX design. Through these processes, the aerodynamic characteristics of Baseline-IX were determined, including the coefficient of lift, coefficient of drag, lift-to-drag ratio, and pitch moment coefficient. This paper compared and discussed both experimental and simulated results with the additional visuals.

Wind tunnel experiment preparation

Experiments were conducted in Flight Technology and Test Center (FTTC) laboratory, College of Engineering, Universiti Teknologi MARA, Shah Alam, using the LST-1 low-speed suction wind tunnel shown in Figure 6. This wind tunnel has a test section area of (0.5 x 0.5 x 1.25) meter and is equipped with a six-component external balance for force and moment measurement. This study used only three longitudinal force components (X, Z, and M) since

the Baseline-IX's wind tunnel model is a half-model type. The wind tunnel model is fabricated by a 3-D printer using fused deposition method (FDM) and has undergone finishing processed to be experiment-ready. Experiments' findings are to validate the results obtained through numerical computational simulations as were similarly done by Apetrei et al. (2020).

A study by Wang et al. said similarity laws are applied to obtain reliable and accurate result where one or several similar parameters constitute the similarity condition (Tai et al., 2023). Wolowicz et al. (1979) reported that similitude requirements must be satisfied to define scaled model experimental aerodynamic data to its full-scale aircraft. Scaling ratio of wind tunnel model may affect changes in Reynolds number and Mach number resulting in large difference between scaled and full-scale model (Tai et al., 2023).

Previous study by Wang et al. in 2019 (Wang et al., 2019) revealed that effects on Mach number and Reynolds number on the similarity motions of wind tunnel's scaled model can be ignored if it satisfies the specifications of Mach number of less than 0.4 and a scaling ratio greater than 1/13. The scaling down of Baseline-IX was done with a rule of satisfying its Reynold number similarity. Experiment was done regarding the prototype (full-scale)'s cruising speed 15 m/s for prototype (full size size). Satisfying the same Reynolds number between both models and test section of the wind tunnel facility, scaled down model was calculated to experiment at airspeed of 36 m/s. Scaled ratio for Baseline-IX is 1:2.4. Below Table 3 summarizes the details of both models.

Table 3. Specifications of Baseline-IX BWB similarity ratio

Specifications	Baseline-IX BWB Scaled Down Model	Baseline-IX BWB Prototype
Chord Length (m)	0.148	0.356
Wingspan (m)	0.350 (half-span)	1.740
Reynolds Number	3.54×10^5	3.54×10^5
Ratio	2.4	1.0

CAD software was used to draft the wind tunnel model, which was then converted into G-codes, and then 3D-printed. The model was sprayed with black matte paint after the finishing process. Baseline-IX's wind tunnel model has a wingspan of 0.35-meters with a reference area of 0.0405 m². Baseline-IX wind tunnel model has a 0.148-meters chord length. The wind tunnel's model specifications are shown in Table 3.

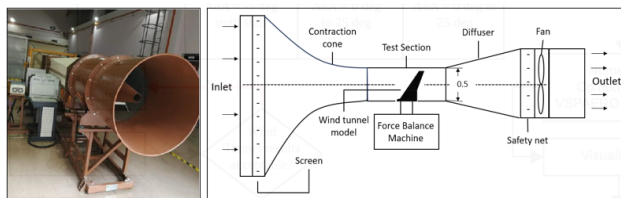
Pitch angle (Angle of Attack) for wind tunnel experiments was increased gradually by one degree and varied from -10 degrees to 25 degrees or until stall. Results of coefficient of lift, coefficient of drag and pitch moment were recorded. The wind tunnel experiments were executed at 3.54×10^5 Reynolds number with 36 m/s airspeed. The wingtip vertical stabilizers on the Baseline-IX wind tunnel model were not fabricated with the model and assumed to have no effect on the longitudinal forces which means that the drag and lift interaction are assumed to be negligible.

The blockage ratio between frontal area of wind tunnel model and the cross-section of wind tunnel's test section, β were calculated to be of value 1.584% which is under 5%. It is admitted that wind tunnels are restricted in recreating flow fields identical to the actual environment. The factors require corrections because of the tunnel walls upon the flow over a model. Every institution with a wind tunnel facility would have the same goal to produce reliable and accurate data (Nasir et al., 2017; Xu et al., 2020). Therefore, additional analysis of corrections was done to the measurements obtained from the wind tunnel experiment. This includes finding the aerodynamic coefficients corrections which are done based on formulas below.

$$\Delta V = \varepsilon_{sb} V_U; \quad (1)$$

$$\varepsilon_{sb} = \frac{K_1 V_U}{S^{3/2}}, \quad (2)$$

where: V_U – uncorrected airspeed, K_1 – for vertical model is 0.52, horizontal model is 0.74, S – working section area.

**Figure 6.** Flight Technology and Test Centre LST-1 Low Speed Wind Tunnel (left); and the schematic of the wind tunnel (right)

Wake blockage:

$$\Delta V = \varepsilon_{wb} V_U; \quad (3)$$

$$\varepsilon_{wb} = \frac{c}{2h} c_{d_u}, \quad (4)$$

where: c_{d_u} – uncorrected coefficient of 2D drag, c – wind tunnel model's length, h – height of the working section.

Streamline curvature correction:

$$\alpha = \alpha_u + \frac{57.3\sigma}{2\pi} (C_{l_u} + 4C_{m_{1/2u}}); \quad (5)$$

$$C_l = C_{l_u} (1 - \sigma - 2\varepsilon); \quad (6)$$

$$C_{m_{1/2}} = C_{m_{1/2u}} (1 - 2\varepsilon) + \frac{\sigma C_l}{4}; \quad (7)$$

$$\sigma = \frac{\pi^2}{48} \left(\frac{c}{h} \right)^2. \quad (8)$$

Total corrected airspeed:

$$\varepsilon_{sb} = \frac{c}{2h} c_{d_{uV=V_U(1+\varepsilon)}}; \quad (9)$$

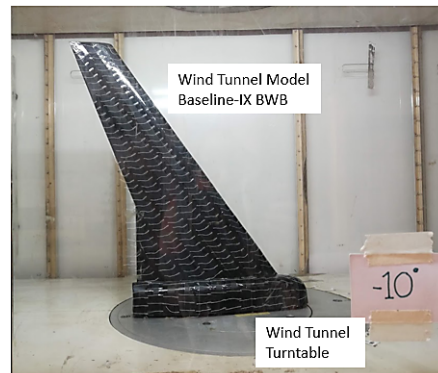
Total corrected drag:

$$C_{d0} = C_{d0u} (1 - 3\varepsilon_{sb} - 2\varepsilon_{wb}). \quad (10)$$

Baseline-IX lift, drag, and moment corrected data were plotted in graphs and discussed in this paper.

Baseline-IX tuft visualization experiment

Tuft visualization experiment was carried out to provide visualization of the flow pattern on the surface of the Baseline-IX wind tunnel model. White lightweight threads 2 cm in length were attached along the wetted surface of the Baseline-IX wind tunnel model as seen in Figure 7. Black surface finishing aids in providing a clearer visualization on tuft behaviour. The test was repeated with angle of attack of -10 degrees until 25 degrees with 1-degree increment and with the same 36 m/s airspeed to the now tuft-equipped model. This experiment was done to observe the behaviour of the tuft on the skin of the Baseline-IX wind tunnel model.

**Figure 7.** Baseline-IX Wind Tunnel model assembly in wind tunnel test section

Numerical computational simulations

Numerical computational simulations were done in two parts. In the first part, the same BWB model and environment of simulation are to mimic the conditions of the wind tunnel experiment for a 1-to-1 comparison. While a second simulation was done on the Baseline-IX prototype model representing the actual size of the aircraft. The simulation utilizes Panel Code Method (PM). Panel Code Method works by superimposing the surface distribution of a model with panels. It is a simplified form of fluid flow equations that are derived from the Navier-Stokes equation (Erickson, 1990). Figure 8 below shows the mesh geometry of Baseline-IX generated before the panel code method simulation.

Panel Code Method is a numerical method based on Prandtl-Glauert equation for solving linear and inviscid flow around aircraft at subsonic or supersonic speed (Erickson, 1990; Mariën & Scholz, 2021; Nasir et al., 2021). Steady subsonic flow and supersonic flow satisfying the Prandtl-Glauert equations which governs incompressible and irrotational flow (Nasir et al., 2017). This Laplace equation is linear and therefore a correct representation of a flow that is considered inviscid and incompressible (Nasir et al., 2021).

Panel code method is lacking in computing the drag force due to its inviscid potential flow computation (Nasir et al., 2021). Therefore, to determine the coefficient of

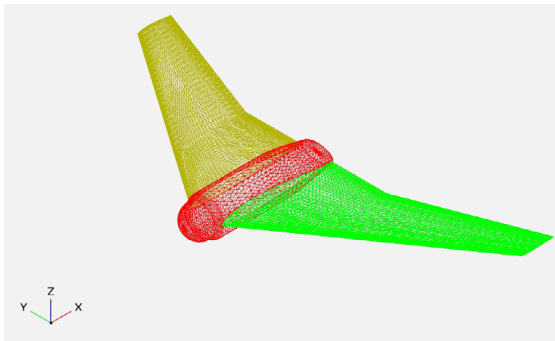


Figure 8. Mesh geometry of Baseline-IX in OpenVSP

drag, the following formula is applied, where C_{Di} is the incidence drag and is added to parasite drag. The parasite drag is calculated below (Nasir et al., 2021):

$$C_D = C_{D0} + C_{Di}; \tag{11}$$

$$C_{D0} = \frac{0.5\rho V^2 S_{wet} C_f FF}{S_{ref}}. \tag{12}$$

Skin friction coefficient, C_f calculations are based on Equation (14) (Nasir et al., 2021):

$$C_f = C_{f,100\%turb} - (C_{f,\%turbulent} \cdot \%laminar) + (C_{f,\%laminar} \cdot \%laminar). \tag{13}$$

The Blasius flat-plate laminar and turbulent approximations are taken into account, where Re is the Reynolds number (Nasir et al., 2021).

Laminar:

$$C_{f,lam} = \frac{1.32824}{\sqrt{Re}}. \tag{14}$$

Turbulent:

$$C_{f,turb} = \frac{0.72}{Re^{1/5}}. \tag{15}$$

While Torenbeek’s form factor estimation was adopted as follows (Nasir et al., 2021).

Wing factor:

$$FF = 1 + 2.7(t/c) + 100(t/c)^4. \tag{16}$$

Fuselage factor:

$$FF = 1 + \frac{2.2}{(l/d)^{1.5}} + \frac{3.8}{(l/d)^3}, \tag{17}$$

where t/c is the airfoil thickness and l/d are the body length-to-diameter ratio (Nasir et al., 2021).

Both the prototype and 1:2.4 half-scaled down simulations were executed with angle of attack (AoA) from 0° until 25°, with an increment of 1.0 degrees each. The AoA of 0° to 25° were decided to represent the same AoA done in wind tunnel experiments. These acquired data

Table 4. Three different models of baseline-IX To accommodate different testing conditions

1:2.4 Scaled Model (Wind Tunnel Experiment)	1:2.4 Scaled Model (Numerical Simulation)	1:1 Prototype (Numerical Simulation)
		
Model ratio of 1:2.4	Model ratio of 1:2.4	Model ratio of 1:1
Half wingspan of 36 cm	Total wingspan of 72.5 cm	Total wingspan of 174 cm
Re = 3.54×10^5	Re = 3.54×10^5	Re = 3.54×10^5
$\alpha = -10^\circ$ until 3°	$\alpha = 0^\circ$ until 25°	$\alpha = 0^\circ$ until 25°
V = 36 m/s	V = 36 m/s	V = 15 m/s
Mach number = 0.105	Mach number = 0.105	Mach number = 0.044

are sufficient to provide input to see the trend with wind tunnel experiments' results. Two types of outputs were produced by numerical computational simulation; the first one is where pressure contour and wake trailing can be observed through visualization results. The second one is where raw average direct data of the simulations are plotted in graphs. The wind tunnel experiment and simulation conditions are explained in Table 4.

Another input obtained from VSPAERO simulations is the coefficient of pressure contour. These contours represent the pressure acting upon the surface of Baseline-IX models (1:2.4 scaled down model and prototype-sized) as the angle of attack increases.

4. Results and discussions

This section discusses the aerodynamic characteristics of Baseline-IX's scaled wind tunnel model, half scaled down simulation model, and prototype model. The results consist of lift coefficient against angle of attack (α), drag coefficient against angle of attack, drag coefficient against lift coefficient, lift-to-drag ratio, and pitch moment coefficient against lift coefficient.

Before the aerodynamics characteristics is discussed, an overview of the results between raw and after corrected wind tunnel results is shown in Figure 9 below. The trendlines showed that the raw wind tunnel's sets of results show a higher slope value of 0.054 compared to the corrected results with 0.047. The percentage difference between raw and corrected wind tunnel results is 14.9%. These findings correlate to Latif's analysis of the planform of Baseline-V between raw and corrected wind tunnel results (Latif et al., 2017).

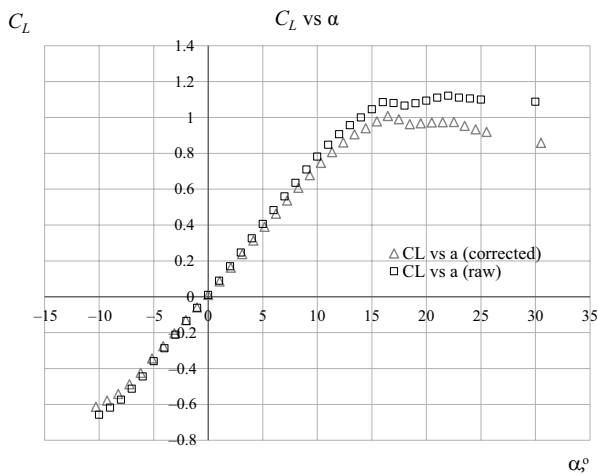


Figure 9. Graph of Lift Coefficient (C_L) versus Angle of Attack (α) between raw and corrected wind tunnel results

Lift coefficient

Figure 10 shows the graph of lift coefficient (C_L) versus angle of attack (α). Based on the figure, all three trend lines of Baseline-IX wind tunnel experiment, scaled-down simu-

lated model, and simulated prototype have similar trend-lines. Simulated results of half scaled down and prototype model seems to be overlapping though the difference in input such as wingspan. At around $\alpha = 17^\circ$, at C_L of 1.02, the simulated models started to shift from their linear progression as seen in the graph plotted. While based on the wind tunnel result, upon reaching the maximum lift at 17 degrees at C_L of 1.01 AoA, the lift starts to fall and rise and then maintains a flat C_L values between $+17^\circ$ and $+22^\circ$. It is believed that at these points the Baseline-IX has already experienced stall. The difference of the value of lift coefficient between wind tunnel experiments and VSPAERO simulation at stall angle of $\alpha = 17^\circ$ is 0.98%.

Wind tunnel experiment's C_L shows higher slope compared to both panel method code simulations with $C_{L\alpha} = +0.066$ per degree compared to simulations' slope of $C_{L\alpha} = +0.060$. Meanwhile, based on the graph in Figure 11, the lift coefficient at zero angle of attack (C_{L0}) for the wind tunnel experiment is just slightly above zero at 0.01 lift coefficient. The C_{L0} for scaled model's simulation is 0.02 and C_{L0} for the Baseline-IX prototype is observed to be at 0.02 as well. Angle of attack at zero lift (α_{0L}) of the Baseline-IX wind tunnel experiment is 0.00 degree, where it does not have any lift. The α_{0L} for simulation results of BWB Baseline-IX scaled-down model and prototype are both at 0.00 degrees.

Summarized results are of lift coefficient (C_L) versus angle of attack (α) is shown in Table 6. The airfoil used in this study possibly contributed to these characteristics. Baseline-IX uses an MH60 airfoil which is a reflex-type airfoil for purpose of a flying wing that has $C_{L0} = 0$ due to its t/c of around 10% (Muta'ali et al., 2020).

Utilizing the numbers extracted from the graph of Lift Coefficient (C_L) versus Angle of Attack (α) as tabulated in Table 5, a mathematical relationship can be established to represent Baseline-IX BWB. If lift is expressed in a linear relationship, it will be expressed as per the following equation.

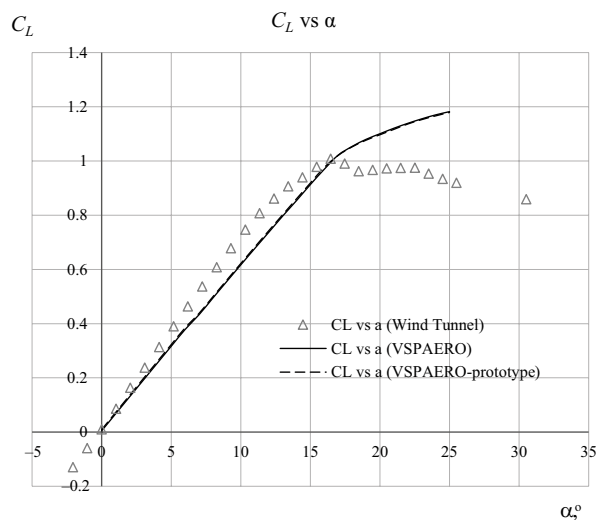


Figure 10. Graph of lift coefficient (C_L) versus angle of attack (α)

Table 5. Results summary from graph of lift coefficient (C_L) versus angle of attack (α)

Parameter	1:2.4 Model Wind Tunnel Experiment	1:2.4 Model VSPAERO Simulation	Prototype VSPAERO Simulation
C_{Lmax}	1.01	1.02	1.02
C_{L0}	0.01	0.02	0.01
α_{0L}	0.00 deg	0.00 deg	0.00 deg
$C_{L\alpha}$	0.07	0.06	0.06

$$C_L = C_{L\alpha} \cdot \alpha + C_{L0} = 0.06\alpha + 0.009. \tag{18}$$

Drag coefficient

Figure 11 shows all the curves of drag coefficient versus angle of attack for the Baseline-IX wind tunnel experiment, half 1:2.4 scaled-down model and full-scale prototype simulation results. Drag coefficient versus angle of attack curves shows parabolic trend lines in all three cases. The drag curve of Baseline-IX wind tunnel experiment case is parabolic for angle of attack lesser than the stall angle of attack.

Meanwhile, Figure 12 below shows a focus result of applicable range of AoA of 0 degrees to 17 degrees extracted from the original graph of Figure 11 discussed previously. Beyond the stall angle of attack at $\alpha = 17^\circ$,

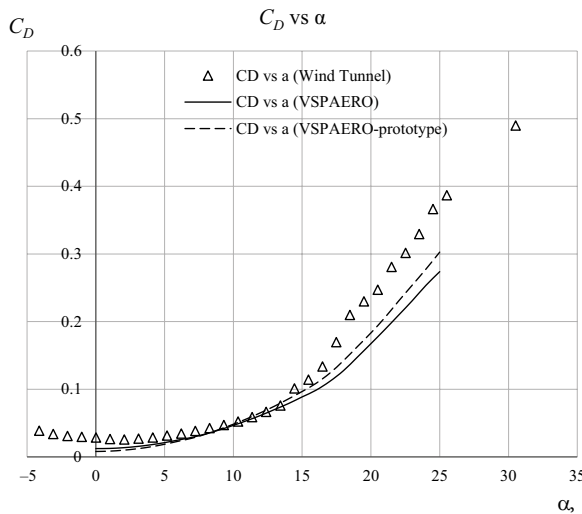


Figure 11. Graph of drag coefficient versus angle of attack

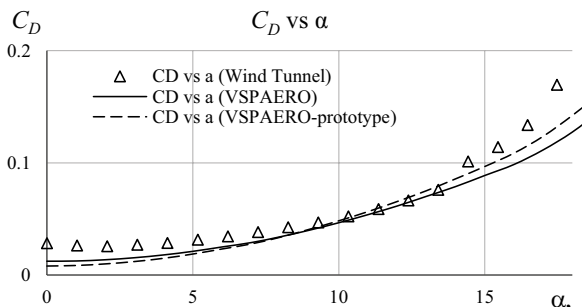


Figure 12. Graph of drag coefficient versus angle of attack (applicable AoA range)

it is observed that the drag coefficient increases rapidly in the wind tunnel experiment. Meanwhile, in both numerical computational simulations between angle of attack 0 degree and 15 degrees, the results seem to closely mimic the wind tunnel experiment results.

Drag polar

Plots lift coefficient (C_L) versus drag coefficient (C_D) as Figure 13 below, also known as drag polar, consist of wind tunnel experiment results and numerical computational simulation results. A shallow parabolic trend is observed on the wind tunnel experiment plots where low drag coefficient is plotted at wide range of angles of attack and rises rapidly as the curve approaches stall angle of attack. The range of low drag coefficient in wind tunnel results is observed to be within -4.0 degrees and 8.0 degrees angle of attack. A steep rise in drag coefficient is observed at lift coefficient lesser than $C_L = -0.3$. A low range of drag coefficient is also observed at $\alpha = 0.0^\circ$ to $+6.0^\circ$ for simulations plots of Baseline-IX of 1:2.4 scaled model and the prototype.

The minimum values of drag recorded for all three cases are 0.026, 0.012 and 0.008 which are for Baseline-IX wind tunnel experiment, 1:2.4 scaled model simulation and prototype simulation, respectively. The curves show that the minimum drag coefficient for wind tunnel does not happen at zero lift coefficient but within range between $C_L = (0.236$ to $0.285)$. However, both simulations plotted the minimum drag values around zero lift coefficient. Parasite drag coefficient or drag at zero lift, C_{D0} is recorded at 0.029 for Baseline-IX’s wind tunnel model. The C_{D0} for computational simulations are 0.0139 and 0.0137 for 1:2.4 scaled model and full-scaled prototype, respectively.

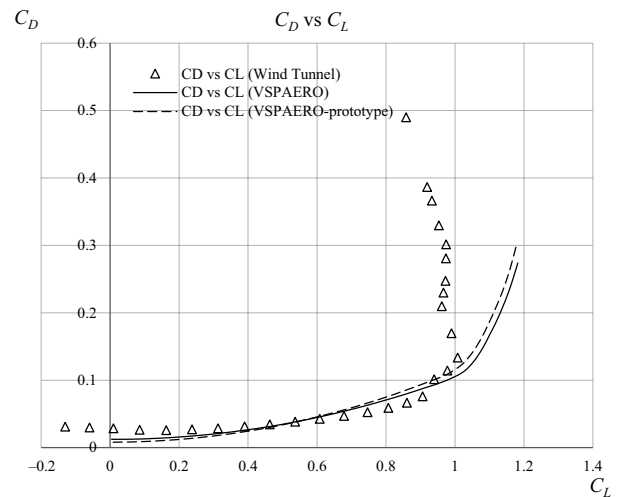


Figure 13. Graph of drag coefficient versus lift coefficient

Based on the graph of drag coefficient versus lift coefficient, the trend line can be represented as:

$$C_D = C_{D0} + k' C_L + k C_L^2. \tag{19}$$

Parameters extracted from the drag polar graph in Figure 13 are drag at zero lift (C_{D0}), and both induced

drag coefficients k' and k . Table 6 shows the information extracted from the parabolic equation obtained from the graph of drag coefficient against lift coefficient.

Table 6. Results summary from graph of drag coefficient (C_D) versus lift coefficient (C_L)

Parameter	1:2.4 Model Wind Tunnel Experiment	1:2.4 Model VSPAERO Simulation	Prototype VSPAERO Simulation
C_{D0}	0.0285	0.0139	0.0137
k	0.2651	0.2756	0.3114
k'	-0.0298	-0.1687	-0.1899

Based on the value in Table 6, the parabolic drag relationship was analyzed by using Baseline-IX prototype's simulation result and it can be represented below.

$$C_D = 0.0137 - 0.1899C_L + 0.3114C_L^2. \quad (20)$$

Lift-to-drag ratio

Figure 14 shows a plot of lift-to-drag ratio (C_D/C_L) versus angle of attack (α) for Baseline-IX wind tunnel experiment, 1:2.4 scaled model and prototype simulations. It can be observed from the following graph that the maximum lift-to-drag ratio of Baseline-IX wind tunnel model is 14.43 at an angle of attack $\alpha = +9.3^\circ$. 1:2.4 scaled down model has the steepest slope among all 3 cases with a maximum lift-to-drag ratio of 15.14 at an angle of attack $\alpha = +6.0^\circ$. Baseline-IX's prototype recorded a maximum lift-to-drag ratio of 17.46 at an angle of attack $\alpha = +5.0^\circ$. The coefficient of lift at maximum lift-to-drag ratio of wind tunnel experiment, 1:2.4 scaled-down model, and prototype's simulations are 0.684, 0.379, and 0.323 respectively.

There is a significant difference in the lift-to-drag ratio between the prototype and 1:2.4 scaled-down model results due to the difference in its chord length. The boundary layer that surrounds the airfoil is known to decrease its thickness as the Reynold number increases, which is relative to the thickness of the chord length. Table 8 shows the results summary obtained from the graph in Figure 14. The reason for such a difference in maximum lift-to-drag ratio between all 3 cases is firstly due to the surface finishing of the Baseline-IX's wind tunnel model. The matte paint finishing may contribute to surface drag during wind tunnel experiments resulting in lower C_L/C_D compared to simulations. Baseline-IX was modelled as having a smooth profile by VSPAERO, under sub-program panel method code where no turbulence model existed. The prototype which has the largest size among the other two will have larger C_L/C_D , resulting in a lower drag on the Baseline-IX prototype. Hence the highest maximum L/D of 17.46. The percentage difference of maximum lift-to-drag ratio between wind tunnel experiment and 1:2.4 scaled-down VSPAERO simulation is 4.9% which is relatively small. Table 7 shows summary for lift-to-drag characteristics for Baseline-IX BWB.

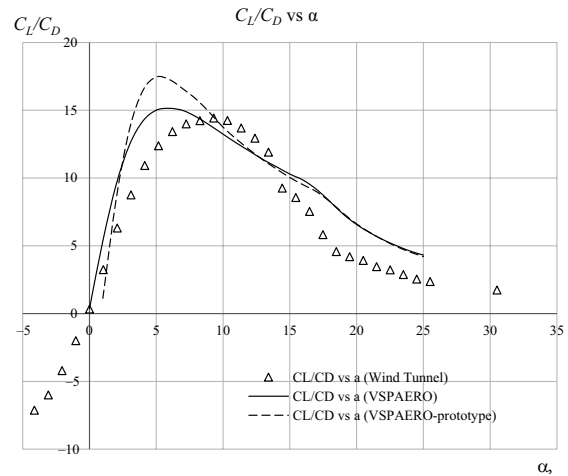


Figure 14. Graph of lift-to-drag ratio versus angle of attack

Table 7. Results summary from graph of lift to drag ratio (C_L/C_D) versus angle of attack (α)

Parameter	1:2.4 Model Wind Tunnel Experiment	1:2.4 Model VSPAERO Simulation	Prototype VSPAERO Simulation
$\frac{C_L}{C_D}$	14.43	15.14	17.46
$\alpha_{L/D}$	+9.3	+6.0	+5.0

Therefore, lift-to-drag ratio:

$$\frac{L}{D} = \frac{C_L}{C_D} = 14.4 \text{ to } 17.5. \quad (21)$$

Pitch Moment Coefficient (C_M) versus Lift Coefficient (C_L)

Figure 15 shows the plot of graph of pitch moment coefficient against lift coefficient for all cases. The moment coefficient is measured at a location of +129 mm from Baseline-IX's leading edge. This C_M versus C_L plot shows all has almost similar and positive magnitude slopes. The linear region of the three cases shows a negative gradient of -0.013, -0.022, and -0.017 for wind tunnel model, 1:2.4 scaled down simulation model, and Baseline-IX prototype, respectively. This specifies that the stick-fixed neutral points are 1.3% mean chord behind the wind tunnel center. Specifically, these are the static margin K_n of Baseline-IX. The slope's percentage difference within the linear region of 1:2.4 scaled down simulation model and wind tunnel experiment are 69.0%.

The trend lines of all three, wind tunnel and both simulation results show a similar negative slope in linear, applicable region, highlighted with red lines in Figure 15. The trim condition is visibly in a negative slope which is considered longitudinally stable. This trim condition can be improved by elevon deflection that increases moment at zero lift thus also increases trim angle of attack to optimal flight condition where L/D is maximum. Pitch moment coefficient versus lift coefficient characteristics summary is presented in Table 8.

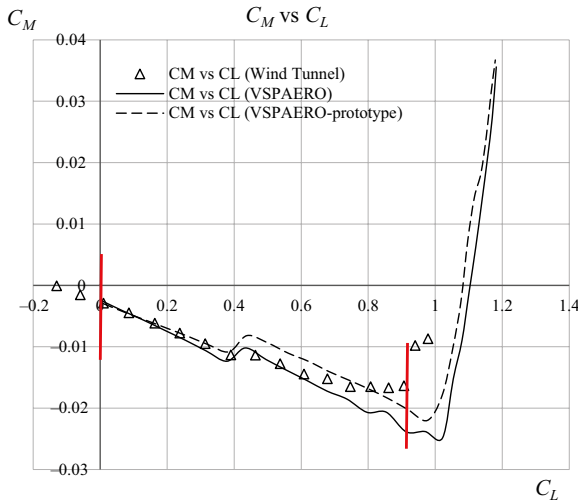


Figure 15. Graph of pitch moment coefficient versus lift coefficient

Table 8. Results summary from graph of pitch moment coefficient (C_D) versus lift coefficient (C_L)

Parameter	1:2.4 Model Wind Tunnel Experiment	1:2.4 Model VSPAERO Simulation	Prototype VSPAERO Simulation
C_{M0}	-0.005	-0.003	0.003
$\frac{dC_M}{dC_L}$	-0.013	-0.022	-0.017

$$C_M = \frac{dC_M}{dC_L} C_L + C_{M0} \tag{22}$$

Prototype’s numerical computational simulation results are used to represent Baseline-IX stability characteristics as the result did not differ much from the wind tunnel experiment. Therefore, a mathematical relationship that can be established to represent the phenomenon is as below.

$$C_M = -0.017C_L + 0.003. \tag{23}$$

Based on C_M vs C_L plot, Baseline-IX’s prototype has a negative slope which is -0.017 . Stability improvement can be made by adding vertical stabilisers and elevons to its control surfaces and is to be implemented to ensure the slope trim is at a positive value.

Baseline-IX tuft and pressure contour visualization

This section discusses the pressure contour obtained by VSPAERO simulations and tuft visualization through wind tunnel experiments. VSPAERO simulations produced pressure contour visualizations which give added information apart from the aerodynamics data. Figure 16 shows the pressure contour visualizations of simulated 1:2.4 model and prototype sized model.

For tuft visualization, white lightweight cotton tufts are attached to the black painted surface of half wind tunnel model for surface flow observation. This helps in detecting regions of unsteady flow and flow separation that occurred instantaneously. Previous plotted results presented that the aerodynamics characteristics between simulations and wind tunnel experiments do not have big differences. The trendlines are almost similar up to its stall region.

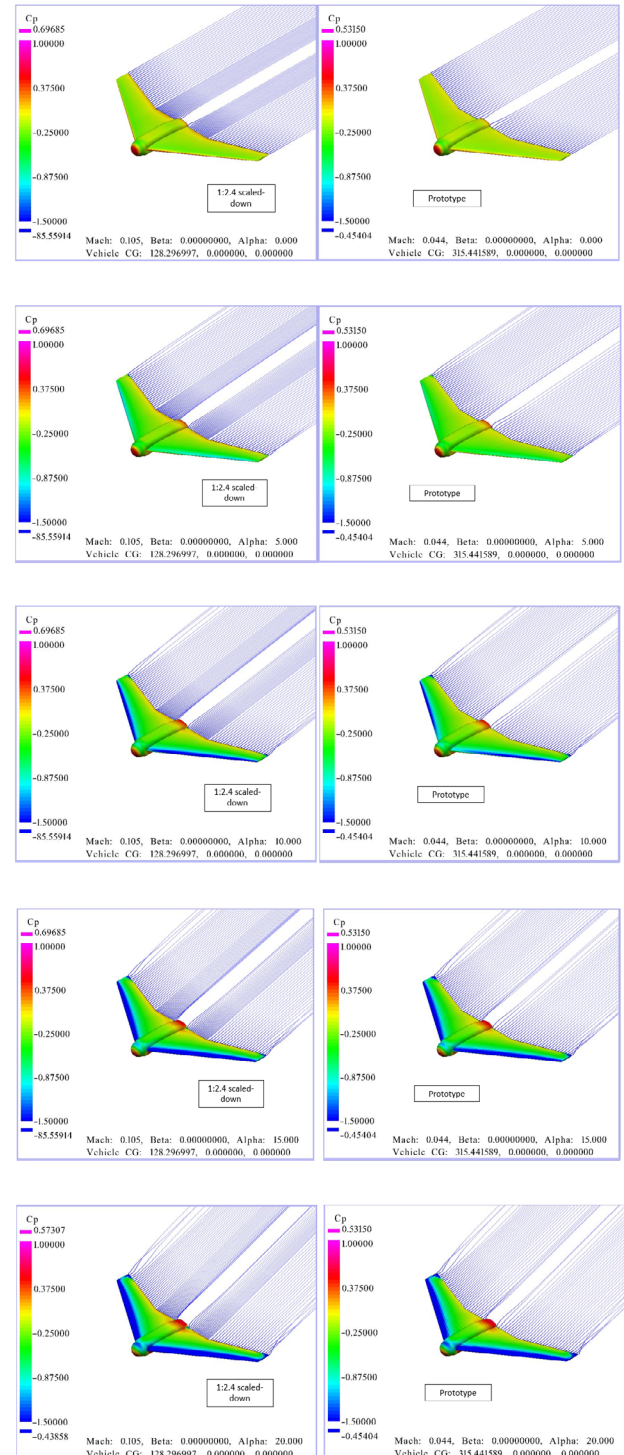


Figure 16. VSPAERO pressure contour visualization from $\alpha = 5^\circ$ to 20°

Observation at zero-degree angle of attack of the Baseline-IX wind tunnel model, the tuft pattern are following the direction of airflow in the wind tunnel test section. The tuft patterns are the same as those observed on the top and bottom of the wind tunnel model shown in Figure 17. Figure 18 shows Baseline-IX 1:2.4 scaled down model and prototype's pressure contour at zero angle of attack. Prototype's pressure contour is seen to be in a lighter shade ($C_p > -0.25$) compared to the scaled-down model. This indicates that the prototype experienced higher pressure on the surface due to its larger wetted surface. In Figure 20, the top and bottom surface's pressure contour's shades are identical to each other. This correlates to white tuft patterns on Figure 19, where the behavior is similar to top and bottom surface as well.

Moreover, at 0-degree AoA, the nose of Baseline-IX is the only region in red due to this is where the coefficient of pressure is higher than the rest of the wetted surface. As the aircraft accelerates, the nose is the first part of the aircraft that is in friction with the air. At this point, the coefficient of pressure is between 0.546 to 1.003 (C_p).

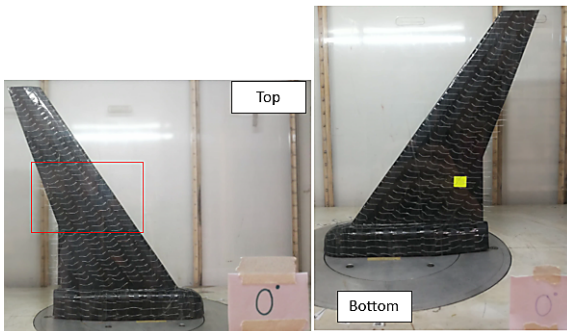


Figure 17. Wind tunnel's tuft flow visualisation at 0-degree AoA

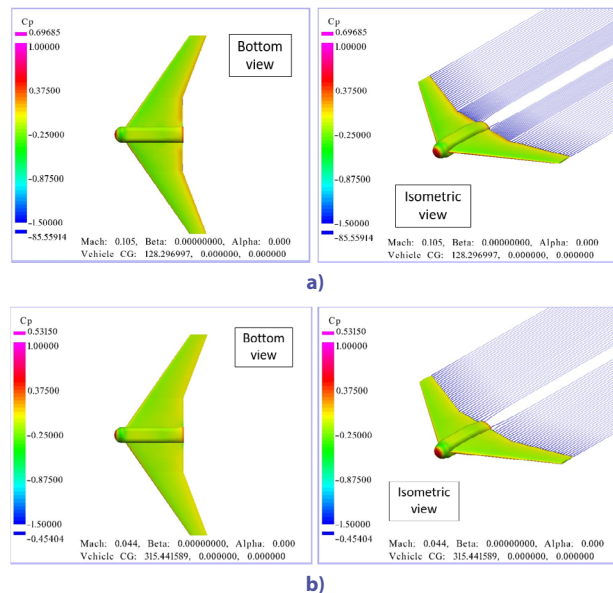


Figure 18. VSPAERO pressure contour visualization at 0-degree AOA: a – wind tunnel scaled model, b – prototype-size model

At 6.0 degrees AoA, higher pressure was acting upon the bottom surfaces of both wind tunnel model and simulation models. As shown in Figure 19, the pattern of mounted white tufts began to change. Boundary layer separation is visible at the leading edge of the bottom of the wind tunnel model. Small curls were developing and visible at the top surface as well as on the trailing edge of the wind tunnel model. This also correlates to pressure contour change in Figure 20a, where the trailing edge of both 1:2.4 scaled and prototype model's bottom surfaces were experiencing higher pressure than the rest of the surface, with $C_p = 0.375$. The same conditions are observed on the pressure contour of prototype-sized model except for the leading edge where it is under higher pressure compared to 1:2.4 scaled model (Figure 20b). The lowest coefficient of pressure experienced by the leading edge of 1:2.4 scaled model model is $C_p = -1.500$.

As the angle of attack increased throughout the experiment, change of tufts pattern was gradually observed. At $\alpha = +12.0$ degrees angle of attack shown in Figure 21, where most of the white tufts of the bottom part of the

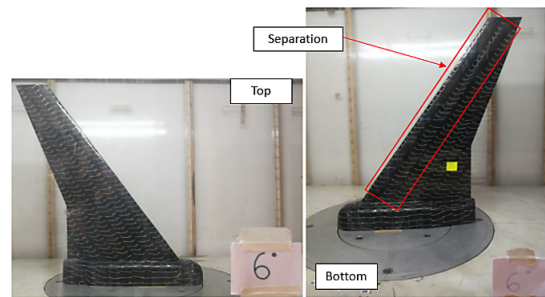


Figure 19. Tuft flow visualisation at 6 degrees AoA

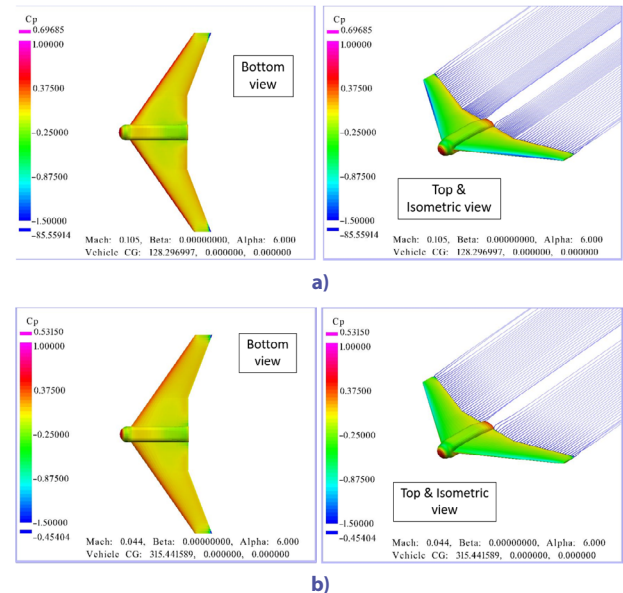


Figure 20. VSPAERO pressure contour visualization at 6 degrees AOA: a – wind tunnel scaled model, b – prototype-size model

wind tunnel model are curling, indicating the region was experiencing flow separation. While the tufts attached on the top surface of the half wind tunnel model were mostly curling at the back of the wings and along the wing tip. In Figure 24, are the pressure contour additional visualizations of 1:24 scaled down model and prototype model. Tuft visualization was supported by panel method visualization result with the same angle of attack. Pressure contour visualization shows that top surface (Figure 22a) experienced higher pressure ($C_p = 0.350$) along the trailing edge just like tuft behaviour shown on top wing surface in Figure 21. The bottom surface of both 1:2.4 scaled down and prototype model have highest pressure along the leading edge ($0.375 \leq C_p \leq 1.00$). This condition is backed up tuft behaviour on bottom surface where the curls are more visible along the leading edge where the flow separations have occurred.

The white threads on the surface of wind tunnel model's curls are visually obvious on both top and bottom surfaces at AoA 17 degrees. These visualizations showed boundary layer separation occurred on top and bottom surfaces. The pressure contour from numerical

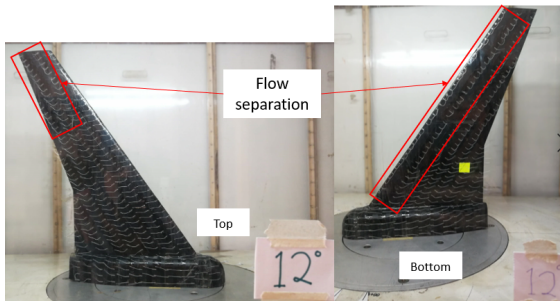


Figure 21. Tuft flow visualisation at 12 degrees AoA

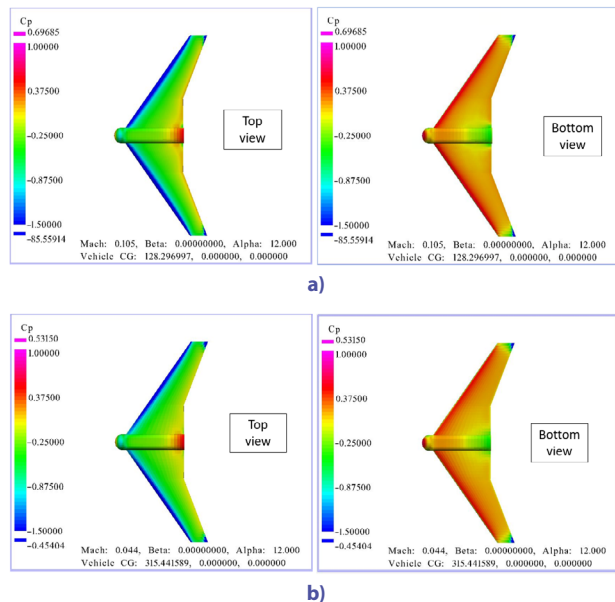


Figure 22. VSPAERO pressure contour visualization at 12 degrees AOA: a – wind tunnel scaled model, b – prototype-size model

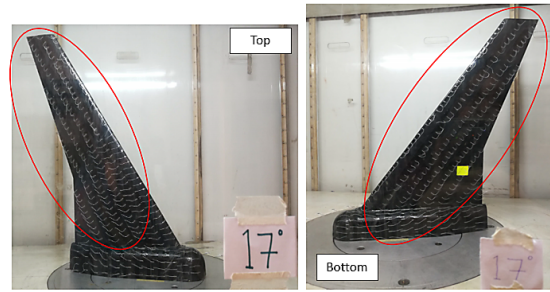


Figure 23. Baseline-IX wind tunnel model's tuft flow visualisation at 17 degrees angle of attack

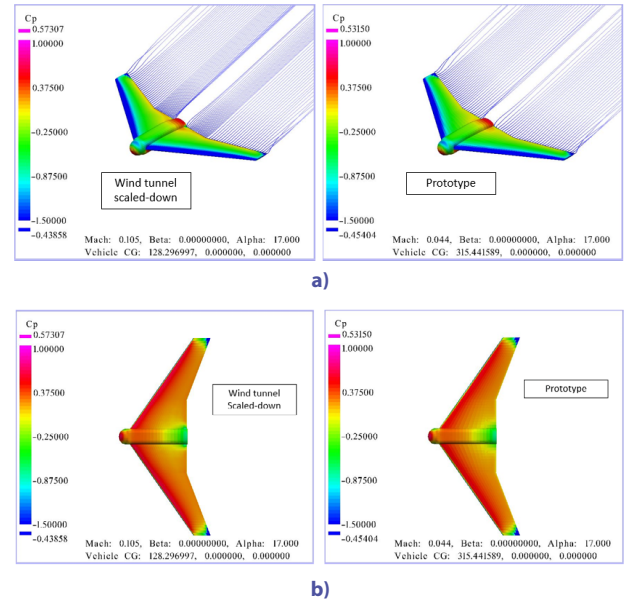


Figure 24. Pressure contour of Baseline-IX: a – scaled-down model at 17 degrees AoA (top view), b – prototype at 17 degrees AoA (top view)

computational simulation in Figure 23 highlights that at $\alpha = +17.0^\circ$, lift starts to decline. The pressure is highest on the wings, just after the leading edge until the trailing edge for both the scaled-down model and prototype (Figure 24a and 24b). The visualizations indicating high pressure decrease as it moves along to the trailing edge. These simulation's visuals and tuft behaviour observations correlate to the stall angle obtained through lift coefficient graph plotted in Figure 11. Figure 24b where high pressure acted upon most bottom surfaces of 1:2.4 scaled down and prototype models ($C_p > 0.375$) were supported by the tuft behavior on bottom surface in Figure 23.

5. Conclusions

The aerodynamic performance and the percentage difference between Baseline-IX with other UAV with similar mission profile shall be concluded. The aerodynamic performance that can be discussed as a common ground is the maximum lift-to-drag ratio (glide ratio) due to the lack of Zipline UAV's aerodynamic performance information. Xu (2017) estimated that Zipline or any other fixed-wing

planform would have a maximum L/D of between 10.0 to 15.0. For this discussion, $C_L/C_D = 15.0$ is considered for Zipline UAV. Due to the larger wetter surface of Baseline-IX, the maximum L/D is 14.09% higher than Zipline UAV even though it is half the size. By comparison to DELAER RX-3 UAV, Baseline-IX is 24.28% difference in maximum lift-to-drag ratio and in a fraction of size.

VSPAERO numerical simulation and wind tunnel experiment of Baseline-IX: both scaled down models show that high percentage difference is seen on the parasite drag at 51.72% and slope of graph for moment coefficient which is at 69.23%. Parasite drag between numerical simulation and wind tunnel experiment resulted in higher percentage which is due to VSPAERO drag value only represent induced drag. The percentage difference of Baseline-IX aerodynamic characteristics has a small difference with lift-to-drag ratio of 4.92%. While the $C_{L_{max}}$ for both methods produce a 1% difference. It can be concluded that VSPAERO is able to produce almost similar results to wind tunnel experiments in terms of few characteristics. However, just like any simulations approach, they lack in getting the precise drag value on a physical model. In terms of producing quick design and understanding overview of a planform, OpenVSP and VSPAERO can be of an assistance, in regard to the findings in this paper.

Further investigation of added winglet to Baseline-IX wind tunnel model is likely to produce a higher ratio of lift-to-drag. For near future improvement on the design, a pair of elevons added on Baseline-IX wings will provide more control surface to the aircraft. Enhancement of fuselage design will give Baseline-IX even more space for cargo. Current compound wing-body design can be blended into a proper blended wing-body design for a smooth transition between body and wing without changing its overall wing planform sweep angle, area, and span. These changes are expected to improve the lift-to-drag ratio significantly due to a reduction in interference drag and lower wetted area. A higher lift-to-drag ratio means better flight performance, particularly longer flight range and endurance. For an electric-powered UAV, this would also mean lighter battery capacity and mass for a given flight range, hence a slower, easier launch.

This research contributes to research by aerodynamicists working on a similar planform to Baseline-IX. This manuscript provides insight into the preliminary design phase of an easy to transport, practical cargo delivery and surveillance BWB UAV. Baseline-IX's planform has the potential to be one of the small UAV to provide cargo delivery and surveillance services just like proven products such as Zipline and DELAER RX-3.

Funding

This research is part of a project funded by BESTARI PERDANA Grant 2018 (600-IRMI/PERDANA 5/3 BESTARI (047/2018)) and SINERGI Grant 2019 (600-IRMI/DANA 5/3/SINERGI (001/2019)).

Author contributions

ABAM has conducted the experimental and simulations work alongside REMN who the principal collaborator is. REMN and WK both provided expert guidance from the moment technical work is conducted and manuscript writing. All authors contributed towards the writing and reviewing of this manuscript. The authors read and approved the final manuscript.

Disclosure statement

The authors declare no conflict or interest. The funders had no role in the design of the study; in the collection, analyses, or interpretation of data; in the writing of the manuscript; or in the decision to publish the results.

Acknowledgements

The authors would like to express gratitude to Universiti Teknologi MARA's Research Management Centre, College of Engineering, School of Mechanical Engineering, and especially to the Dean and Deputy Dean (Research and Industrial Network) for grant money and various support. Our special thanks are dedicated to Mr. Zulhilmi Haron, Mr. Shahrean Zainurin, Mr. Zulfazly, Mr. M. Aiman, Mr. Tajul Arus, and other research students under Flight Technology and Test Research Group, Universiti Teknologi MARA, Shah Alam.

References

- Ammar, S., Legros, C., & Trépanier, J. (2017). Conceptual design, performance and stability analysis of a 200 passengers Blended Wing Body aircraft. *Aerospace Science and Technology*, 71, 325–336. <https://doi.org/10.1016/j.ast.2017.09.037>
- Apetrei, R. M., Ciobaca, V., Curiel-Sosa, J. L., & Qin, N. (2020). Unsteady shock front waviness in shock-buffet of transonic aircraft. *Advances in Aerodynamics*, 2(1). <https://doi.org/10.1186/s42774-020-00034-x>
- Aprovitola, A., Aurisicchio, F., Di Nuzzo, P. E., Pezzella, G., & Viviani, A. (2022). Low speed aerodynamic analysis of the N2A hybrid wing-body. *Aerospace*, 9(2), Article 89. <https://doi.org/10.3390/aerospace9020089>
- Arora, A., Das, S., & Kumar, P. (2023). Flow field investigation of a blended wing body in low speeds. *Journal of Applied Fluid Mechanics*, 16(4), 794–804. <https://doi.org/10.47176/jafm.16.04.1475>
- Chen, Z., Zhang, M., Chen, Y., Sang, W., Tan, Z., Li, D., & Zhang, B. (2019). Assessment on critical technologies for conceptual design of blended-wing-body civil aircraft. *Chinese Journal of Aeronautics*, 32(8), 1797–1827. <https://doi.org/10.1016/j.cja.2019.06.006>
- Dehpanah, P., & Nejat, A. (2015). The aerodynamic design evaluation of a blended-wing-body configuration. *Aerospace Science and Technology*, 43, 96–110. <https://doi.org/10.1016/j.ast.2015.02.015>
- Dimitriou, S., Kapsalis, S., Dimopoulos, T., Mitridis, D., Pouchias, K., Panagiotou, P., & Yakinthos, K. (2022). Preliminary design of a BWB UAV for highway traffic monitoring. *IOP Conference Series: Materials Science and Engineering*, 1226(1), Article 012010. <https://doi.org/10.1088/1757-899X/1226/1/012010>

- Erickson, L. L. (1990). Panel methods – an introduction. In NASA *Technical Paper 2995*. NASA.
- Jemitola, P. O., & Okonwo, P. P. (2022). An analysis of aerodynamic design issues of box wing aircraft. *Global Journal of Researches in Engineering*, 22(1).
- Kapsalis, S., Panagiotou, P., & Yakinthos, K. (2021). CFD-aided optimization of a tactical Blended-Wing-Body UAV platform using the Taguchi method. *Aerospace Science and Technology*, 108, Article 106395. <https://doi.org/10.1016/j.ast.2020.106395>
- Karpenko, M., & Nugaras, J. (2022). Vibration damping characteristics of the cork-based composite material in line with frequency analysis. *Journal of Theoretical and Applied Mechanics*, 60(4), 593–602. <https://doi.org/10.15632/jtam-pl/152970>
- Karpenko, M., Stosiak, M., Deptula, A., Urbanowicz, K., Nugaras, J., Krolczyk, G., & Zak, K. (2023). Performance evaluation of extruded polystyrene foam for aerospace engineering applications using frequency analyses. *The International Journal of Advanced Manufacturing Technology*, 126(11–12), 5515–5526. <https://doi.org/10.1007/s00170-023-11503-0>
- Kusumohadi, C. S., Basri, S., & Rafie, A. S. M. (2021). Conceptual design of Wau Bulan UAV. *IOP Conference Series: Materials Science and Engineering*, 1098(6), Article 062106. <https://doi.org/10.1088/1757-899X/1098/6/062106>
- Latif, M. Z. A. A., Ahmad, M. A., Nasir, R. E. M., Wisnoe, W., & Saad, M. R. (2017). An analysis on 45° sweep tail angle for blended wing body aircraft to the aerodynamics coefficients by wind tunnel experiment. *IOP Conference Series: Materials Science and Engineering*, 270(1). <https://doi.org/10.1088/1757-899X/270/1/012001>
- Li, P., Zhang, B., Chen, Y., Yuan, C., & Lin, Y. (2012). Aerodynamic design methodology for blended wing body transport. *Chinese Journal of Aeronautics*, 25(4), 508–516. [https://doi.org/10.1016/S1000-9361\(11\)60414-7](https://doi.org/10.1016/S1000-9361(11)60414-7)
- Liebeck, R. H. (2004). Design of the blended wing body subsonic transport. *Journal of Aircraft*, 41(1). <https://doi.org/10.2514/1.9084>
- Mariën, F., & Scholz, I. D. (2021). *Software Testing: VSPAERO* [Hamburg University of Applied Science]. Harvard Dataverse. <https://doi.org/10.7910/DVN/0S1R14>
- Mohammad Zadeh, P., & Sayadi, M. (2018). An efficient aerodynamic shape optimization of blended wing body UAV using multi-fidelity models. *Chinese Journal of Aeronautics*, 31(6), 1165–1180. <https://doi.org/10.1016/j.cja.2018.04.004>
- Muta'ali, A. B. A., Nasir, R. E. M., Wisnoe, W., & Kuntjoro, W. (2020). Aerodynamic performance of a tail-less blended wing-body small transport aircraft. *Journal of Advanced Research in Fluid Mechanics and Thermal Sciences*, 66(1).
- Nasir, R. E. M., Ahmad, A. M., Latif, Z. A. A., Saad, R. M., & Kuntjoro, W. (2017). Experimental result analysis for scaled model of UiTM tailless blended wing-body (BWB) Baseline 7 unmanned aerial vehicle (UAV). *IOP Conference Series: Materials Science and Engineering*, 270(1). <https://doi.org/10.1088/1757-899X/270/1/012005>
- Nasir, R. E. M., Tajuddin, N. F., Muta'ali, A. B. A., Kuntjoro, W., Wisnoe, W., & Romli, F. I. (2021). The effect of inboard and outboard wing sweep angles to lift-to-drag ratio of a compound wing-body using panel code. *Journal of Aeronautics, Astronautics and Aviation*, 53(2), 155–164. [https://doi.org/10.6125/JoAAA.202106_53\(2\).07](https://doi.org/10.6125/JoAAA.202106_53(2).07)
- Okonkwo, P., & Smith, H. (2016). Review of evolving trends in blended wing body aircraft design. *Progress in Aerospace Sciences*, 82, 1–23. <https://doi.org/10.1016/j.paerosci.2015.12.002>
- Panagiotou, P., Antoniou, S., & Yakinthos, K. (2022). Cant angle morphing winglets investigation for the enhancement of the aerodynamic, stability and performance characteristics of a tactical Blended-Wing-Body UAV. *Aerospace Science and Technology*, 123. <https://doi.org/10.1016/j.ast.2022.107467>
- Panagiotou, P., Fotiadis-Karras, S., & Yakinthos, K. (2018). Conceptual design of a Blended Wing Body MALE UAV. *Aerospace Science and Technology*, 73, 32–47. <https://doi.org/10.1016/j.ast.2017.11.032>
- Papadopoulos, C., Mitridis, D., & Yakinthos, K. (2022). Conceptual design of a novel unmanned ground effect vehicle (UGEV) and flow control integration study. *Drones*, 6(1). <https://doi.org/10.3390/drones6010025>
- Qin, N., Vavalle, A., Le Moigne, A., Laban, M., Hackett, K., & Weinerfelt, P. (2004). Aerodynamic considerations of blended wing body aircraft. *Progress in Aerospace Sciences*, 40(6), 321–343. <https://doi.org/10.1016/j.paerosci.2004.08.001>
- Raja, V., Murugesan, R., Solaippan, S. K., Arputharaj, B. S., Rajendran, P., Al-Bonsrulah, H. A. Z., Thakur, D., Razak, A., Buradi, A., & Ketema, A. (2023). Design, computational aerodynamic, aerostuctural, and control stability investigations of VTOL-configured hybrid blended wing body-based unmanned aerial vehicle for intruder inspections. *International Journal of Aerospace Engineering*, 2023. <https://doi.org/10.1155/2023/9699908>
- Tai, S., Wang, L., Wang, Y., Bu, C., Yue, T., & Liu, H. (2023). Research on dynamic characteristics analysis and control law design method of model aircraft in wind tunnel-based virtual flight testing. *Journal of Aerospace Engineering*, 36(3). <https://doi.org/10.1061/JAEEZ.ASENG-4565>
- Viviani, A., Arovitola, A., Iuspa, L., & Pezzella, G. (2020). Low speed longitudinal aerodynamics of a blended wing-body re-entry vehicle. *Aerospace Science and Technology*, 107. <https://doi.org/10.1016/j.ast.2020.106303>
- Wang, G., Zhang, M., Tao, Y., Li, J., Li, D., Zhang, Y., Yuan, C., Sang, W., & Zhang, B. (2020). Research on analytical scaling method and scale effects for subscale flight test of blended wing body civil aircraft. *Aerospace Science and Technology*, 106. <https://doi.org/10.1016/j.ast.2020.106114>
- Wang, L., Zuo, X., Liu, H., Yue, T., Jia, X., & You, J. (2019). Flying qualities evaluation criteria design for scaled-model aircraft based on similarity theory. *Aerospace Science and Technology*, 90, 209–221. <https://doi.org/10.1016/j.ast.2019.04.032>
- Waters, S. M., Voskuil, M., Veldhuis, L. L. M., & Geuskens, F. J. J. M. (2013). Control allocation performance for blended wing body aircraft and its impact on control surface design. *Aerospace Science and Technology*, 29(1), 18–27. <https://doi.org/10.1016/j.ast.2013.01.004>
- Wolowicz, C. H., Bowman, J. S., & Gilbert, W. P. (1979). *Similitude requirements and scaling relationships as applied to model testing*. NASA. <https://ntrs.nasa.gov/api/citations/19790022005/downloads/19790022005.pdf>
- Xu, J. (2017). *Design perspectives on delivery drones*. RAND. <https://doi.org/10.7249/RR1718.2>
- Xu, X., Li, Q., Liu, D., Cheng, K., & Chen, D. (2020). Geometric effects analysis and verification of v-shaped support interference on blended wing body aircraft. *Applied Sciences (Switzerland)*, 10(5), Article 1596. <https://doi.org/10.3390/app10051596>
- Zeng, C., Abnous, R., Gabani, K., Chowdhury, S., & Maldonado, V. (2020). A new tilt-arm transitioning unmanned aerial vehicle: Introduction and conceptual design. *Aerospace Science and Technology*, 99, Article 105755. <https://doi.org/10.1016/j.ast.2020.105755>
- Zipline. (2022). *About Zipline: Zipline fact sheet*. <https://www.flyzipline.com/about/zipline-fact-sheet>

Notations

Symbols

C_D – Drag coefficient;
 C_{D0} – parasite drag;
 C_{Di} – incidence drag;
 C_L – lift coefficient;
 C_{L0} – coefficient of lift at 0° AoA;
 C_{Lmax} maximum lift coefficient;
 C_M – coefficient of moment;
 C_{M0} – coefficient of moment at zero lift;
 C_p – coefficient of pressure;
 S – planform area;
 α – angle of attack;
 α_{0L} – angle of attack at zero lift;
 $\alpha_{\frac{L}{D}}$ – angle of attack at maximum L/D.

Sub-/superscripts

AoA – angle of attack;
 BWB – blended wing-body;
 L/D – lift-to-drag ratio;
 $LST-1$ – low speed wind tunnel;
 Re – Reynolds number;
 UAS – unmanned aerial system;
 UAV – unmanned aerial vehicle.